Particuology 115 (2026) 1–14

Contents lists available at ScienceDirect

Particuology

journal homepage: www.elsevier.com/locate/partic

Agglomeration-abrasion-oriented strategy for spherical crystallization design: The case of aluminum fluoride

Shubo Liu[a,1], Jiantao Yan[a,1], Shengzhe Jia[a], Ke Yu[c], Huamin Yin[c], Shulin Chen[c], Weiwei Tang[a,b,*], Junbo Gong[a,b,**]

[a] School of Chemical Engineering and Technology, State Key Laboratory of Chemical Engineering and Low-Carbon Technology, The Co-Innovation Center of Chemistry and Chemical Engineering of Tianjin, Tianjin University, Tianjin, 300072, China
[b] Haihe Laboratory of Sustainable Chemical Transformations, Tianjin, 300192, China
[c] Yunnan Yuntianhua Fluorine Chemical Co., Ltd, Kunming, 650228, China

HIGHLIGHTS

- Microcrystals spontaneously adhere and embed in solution to form dense AFT spheres.
- An additive-free agglomeration-abrasion strategy can be used to prepare AFT spheres.
- RSM quantified multi-factor interactions, yielding AFT spheres of 90.7% circularity.
- Synergy of temperature and stirring drives the AFT spherical crystallization process.
- Optimized spherical AFT exhibits significantly improved powder properties.

GRAPHICAL ABSTRACT

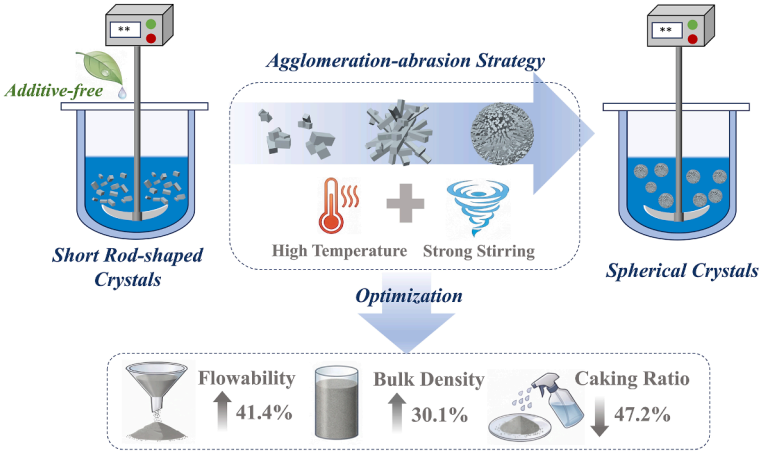

ARTICLE INFO

Keywords:
Spherical particles
Aluminum fluoride trihydrate
Response surface methodology
Spherical agglomeration

ABSTRACT

Aluminum fluoride (AlF_3) is an essential industrial material widely used in aluminum electrolysis and ceramics, yet its performance depends critically on the powder properties of its precursor, aluminum fluoride trihydrate (AFT). However, conventional AFT crystals suffer from irregular morphologies, leading to poor flowability, low bulk density, and severe caking. In this study, we successfully prepared highly spherical AFT particles in an additive-free aqueous solution. Through integrated offline and in-situ analyses, we elucidated the AFT spherical

This article is part of a special issue entitled: Crystalline Porous Particles published in Particuology.

* Corresponding author. School of Chemical Engineering and Technology, State Key Laboratory of Chemical Engineering and Low-Carbon Technology, The Co-Innovation Center of Chemistry and Chemical Engineering of Tianjin, Tianjin University, Tianjin, 300072, China.
** Corresponding author. School of Chemical Engineering and Technology, State Key Laboratory of Chemical Engineering and Low-Carbon Technology, The Co-Innovation Center of Chemistry and Chemical Engineering of Tianjin, Tianjin University, Tianjin, 300072, China.
E-mail addresses: wwtang@tju.edu.cn (W. Tang), junbo_gong@tju.edu.cn (J. Gong).
[1] These authors contributed equally to this work.

https://doi.org/10.1016/j.partic.2026.04.025
Received 12 February 2026; Received in revised form 16 March 2026; Accepted 20 April 2026
Available online 12 May 2026
1674-2001/© 2026 Chinese Society of Particuology and Institute of Process Engineering, Chinese Academy of Sciences. Published by Elsevier B.V. All rights are reserved, including those for text and data mining, AI training, and similar technologies.

agglomeration mechanism dominated by an "agglomeration-abrasion" process. Guided by this mechanism, key process parameters, including temperature, stirring rate, and residence time, were systematically optimized using response surface methodology. Under the optimized conditions, the resulting AFT particles achieved an average circularity of 90.74% and a high yield of 85.7%. Compared to commercial powders, the optimized spherical AFT exhibited maximum improvements of 30.1% in bulk density and 41.4% in flowability, along with significantly enhanced anti-caking properties. The combination of spherical morphology and high yield enhances batch capacity while offering potential for continuous production, providing a green and cost-effective route for the industrial manufacturing of high-quality AFT powders.

1. Introduction

Spherical crystal morphology, governed by the interplay of kinetics and thermodynamics, provides superior bulk powder properties (Lai et al., 2021). The high geometric symmetry minimizes specific surface area, interparticle friction, and mechanical interlocking, thereby enhancing flowability and packing density. Furthermore, this isotropic morphology also reduces hygroscopicity and caking, improving overall storage and application stability (Stirk et al., 2022). Although traditional crystallization and granulation in separate units for spherulite preparation have been reported (Passerini et al., 2010), their development has been limited due to complex processes, and poor sphericity and compactness of the resulting products. In recent years, there has been a growing interest in directly obtaining satisfactory spherical crystals through the crystallization process. For instance, Yang et al. (2015) produced spherical L-tryptophan crystals by adding gelatin as an additive to the crystallization process. Sun et al. (2021) obtained spherical crystals of drug molecules such as ibuprofen, praziquantel, and menthol based on an oiling-out mechanism. Additionally, the spherical crystallization technique coupling crystallization and granulation using a ternary solvent system (good solvent–anti-solvent–bridging liquid) has also been extensively documented (Yu et al., 2021). For example, Shinde and Mohite (2020) employed a quasi-emulsion solvent diffusion method to produce spherical agglomerates of oxcarbazepine, and Yoshiaki et al. (1982) applied spherical agglomeration technology to prepare spherical salicylic acid particles in a miscible solvent system of water, ethanol, and chloroform. However, due to high consumption and serious environmental pollution caused by extensive organic solvent usage, the development of these techniques has been restricted.

Additive-free and environmentally friendly spherical crystallization methods have attracted widespread attention, particularly in the field of inorganic salts. For instance, spherical drug crystals of ammonium sulfate with excellent powder properties and sustained-release functionality can be obtained through temperature-controlled continuous abrasion and dissolution (Li et al., 2024). Alternatively, by adjusting temperature and stirring rate, the agglomeration–dissolution process of potassium peroxymonosulfate compound salt can be optimized to produce highly flowable, large-sized spherical crystals (Feng et al., 2023). Moreover, spherical KCl particles with anti-caking functionality can be prepared during cooling crystallization via agglomeration and stirring-induced abrasion (Jin et al., 2018). While inorganic spherical crystals offer significant industrial advantages such as anti-fouling properties, enhanced transport efficiency, and improved filtration and washing performance, their fabrication and mechanistic studies remain considerably less explored compared to organic spherical crystals. Therefore, extending spherical crystallization technology to inorganic salts represents a necessary and promising area for development.

Aluminum fluoride trihydrate (AFT) is a key precursor in the production of aluminum fluoride (AlF_3), a critical material in metallurgy used not only as a flux in the electrolytic smelting and refining of aluminum metal but also in ceramics, specialty glasses, and catalysts (Hou et al., 2017; Kubiňáková et al., 2018). AFT is typically produced by the reaction crystallization between fluorosilicic acid solution and solid aluminum hydroxide. Compared to the highly hazardous traditional hydrofluoric acid route, the wet-process utilizing fluorosilicic acid as a raw material is recognized as a green and cost-effective industrial pathway for fluorine waste recovery during phosphoric acid production (Long et al., 2018). Because of its environmental and economic advantages, optimizing the crystallization process within this specific route holds potential for large-scale industrial application. However, fundamental research on the crystallization process of AFT remains notably insufficient in this route due to scarce physicochemical data and demanding solution crystallization conditions. This makes it highly challenging to effectively regulate the reaction crystallization, directly hindering the preparation of AFT with superior powder properties and the development of high-efficiency production processes. Although early studies on different growth stages of AFT have been preliminarily reported (Mahmoud & Abbas, 2005), research on crystal morphology evolution, particle size distribution, and agglomeration mechanism is still limited and unclear. The knowledge gap results in unreasonable crystallization processes, which facilitates the formation of a large amount of irregular and fine AFT crystals during crystallization and causes severe scaling issues (Carpin et al., 2017). Moreover, the mother liquor from conventional crystallization, due to its low efficiency, retains a high solute content, which constitutes a significant waste of raw materials. In general, these issues pose challenges to continuous industrial production. The resulting irregular products exhibit low bulk density and poor flowability, accompanied by high caking tendency and moisture content (Wang et al., 2017), which consequently require excessive energy consumption during the calcination process to produce aluminum fluoride. Therefore, this study aims to improve the particle morphology of AFT via spherical crystallization, thereby resolving its poor powder properties and overcoming industrial production bottlenecks. Furthermore, given that the spherical crystallization of inorganic salts currently relies on complex procedural steps, this work utilizes AFT as a typical case to explore a green spheronization pathway applicable to the broader inorganic salt field through mechanistic investigations.

To date, no studies on the preparation of spherical AFT crystals have been reported. To fill this gap, this study developed a completely additive-free "agglomeration-abrasion" strategy for the direct preparation of spherical AFT crystals in aqueous solution. By combining offline and in-situ analyses, we clearly elucidated a novel dynamic mechanism, revealing that temperature-driven crystallization kinetics and fluid shear from stirring synergistically govern the transition from loose clusters to compact spheres. Building upon this, response surface methodology was utilized to quantify the complex interactions among process parameters, achieving the precise design of spherical AFT. This method was specifically chosen to provide a green, simplified and feasible spheronization pathway of AFT. Ultimately, the optimized spherical AFT exhibited maximum improvements of 30.1% in bulk density and 41.4% in flowability while maintaining a high yield. This work fundamentally overcomes the caking and flow resistance issues of commercial products, thereby offering a reliable and efficient approach for continuous industrial production.

2. Experiments and methods

2.1. Materials

H_2SiF_6 (15 wt%) and $Al(OH)_3$ (AR, powder) used in experiments

were provided by Yunnan Yuntianhua Fluorine Chemical Co., Ltd. (China). For performance comparison, two types of commercial AFT products were utilized as references: commercial product 1 was purchased from Kaimate Tianjin Chemical Technology Co., Ltd. (China), and commercial product 2 is a current industrial product obtained from Yunnan Yuntianhua Fluorine Chemical Co., Ltd. (China). The deionized water used in the experiments was prepared via a reverse osmosis and ion-exchange system, with a conductivity of approximately 8 μS/cm, and was employed to prepare the AFT saturated solution. All chemicals were employed as received.

2.2. Preparation of AlF_3 supersaturated solution

In this study, the reaction crystallization between H_2SiF_6 and $Al(OH)_3$ was adopted. This route entirely avoids the hazards of HF, making the developed spherical crystallization strategy highly compatible with practical industrial scale-up. Guided by this route, a supersaturated aqueous solution of AlF_3 was first prepared to provide the essential environment for subsequent crystallization.

Initially, a specific volume of 15 wt% H_2SiF_6 solution was added into a 300 mL glass crystallizer and the amount of H_2SiF_6 in this solution provided a 3 mol% stoichiometric excess to ensure the complete conversion of $Al(OH)_3$ and emulate the industrial process. The crystallizer was equipped with an external temperature controller (±0.01 K, CF41, Julabo, Germany) and a mechanical stirrer (WB-2000C, Julabo, Germany). The H_2SiF_6 solution was heated to 90 °C within 30 min in the crystallizer and then maintained at this temperature for 10 min to ensure uniform heating. Subsequently, $Al(OH)_3$ powder was immediately added into the crystallizer which was then carefully sealed. The mixture was allowed to react at 90 °C for 15 min. During this period, the stirring rate was set at 300 rpm to enhance mass transfer and ensure a complete reaction. The reaction process was as follows (Chen et al., 2021):

$$3\ H_2SiF_6 + 6\ Al(OH)_3 \rightarrow 6\ AlF_3 + 3\ SiO_2\downarrow + 12\ H_2O$$

Upon completion, the suspension was rapidly vacuum-filtered at room temperature. A Büchner funnel equipped with double-layer filter paper was used to remove the solid silica (SiO_2) byproduct. This filtration step was repeated twice to ensure a perfectly clear AlF_3 supersaturated mother liquor was collected. The pH of this solution was finally maintained at approximately 1.5. It should be emphasized that the AlF_3 solution maintains a metastable state for an extended period at low temperatures (Nielsen & Altintas, 1984), and thereby no crystallization was observed during the room-temperature filtration stage.

2.3. Batch constant-temperature crystallization experiments of AFT

The clear AlF_3 supersaturated mother liquor rich in AlF_3 obtained from the previous step was retained in the glass crystallizer for batch crystallization. Firstly, the solution was heated to the designated target temperature (50, 60, 70, 80, or 90 °C) and once the target temperature was reached, the mechanical stirrer was activated at a specific rate (50, 150, 250, or 450 rpm) to initiate the crystallization process. After stirring the supersaturated aqueous solution for several hours at a certain temperature, a large number of AFT particles were precipitated. Furthermore, an attempt was made to add 20 g/L of crystal seeds with different particle sizes to the mother liquor of AlF_3 to explore its impact on product quality. More experimental details were summarized in Supplementary Table S1. After crystallization, the resulting suspension was subjected to vacuum filtration as described in Section 2.2. The collected wet AFT paste was transferred onto a petri dish and placed in a drying oven at 50 °C for 24 h to completely remove residual moisture.

2.4. Study of spherical agglomeration process

Spherical AFT particles were successfully prepared primarily through rapid agglomeration of AFT caused by high temperature, as well as the abrasion induced by the shear force generated by stirring. The nucleation and growth process of AFT was controlled by setting different temperatures, while the shear force of that was adjusted by controlling the stirring rate.

2.4.1. Investigation of agglomeration and spherical crystallization processes

EasyViewer 400 was responsible for capturing information on changes in crystal chord length, counts, and morphology during the conventional crystallization process of AFT. And SEM was used to obtain images of AFT at different agglomeration stages and product morphology under different crystallization conditions.

2.4.2. Response surface methodology

Response surface methodology (RSM) employs a multivariate quadratic regression equation to model the functional relationship between factors and response values. By analyzing the regression equation, optimal process parameters can be identified. RSM requires fewer experiments, shortens the research cycle, and yields regression models with higher accuracy. Furthermore, it can examine interactions among multiple factors and quantify the contribution of each factor to the performance indicators (Zi et al., 2022). As such, RSM serves as an effective approach for optimizing process conditions, identifying optimal operating points, and analyzing key influencing factors.

In this study, the calculation procedure was divided into experimental design, model fitting, and statistical validation. We used the statistical Box-Behnken design (BBD) to further comprehensively analyze and compare the key factors (temperature, stirring rate, and residence time) affecting the circularity of AFT. These three independent variables were coded at three specific levels (−1, 0, 1), with detailed experimental factors and levels summarized in Table 1.

Based on the BBD principles, the experimental calculation matrix was systematically constructed. The total number of experimental runs (N) is calculated according to the following equation (Ferreira et al., 2007):

$$N = 2k(k-1) + C_0 \quad (1)$$

where k represents the number of independent factors and C_0 represents the number of central points. For our three-factor system ($k = 3$) with five central points ($C_0 = 5$), the mathematical design generated a total of 17 distinct operational runs (Table S2). This specific configuration consisted of 12 factorial points to evaluate the main effects, alongside 5 central points to estimate the pure experimental error. The experimental design matrix and subsequent statistical calculations were executed using the Design-Expert software (version 8.0.6). The experimental data obtained from these 17 runs were utilized to mathematically quantify the interactive effects and fit a generalized second-order polynomial regression equation. This empirical calculation model is expressed as follows (Bezerra et al., 2008):

$$Y = \beta_0 + \sum_{i=1}^{3}\beta_i X_i + \sum_{i=1}^{3}\beta_{ii} X_i^2 + \sum_{i<j}^{3}\beta_{ij} X_i X_j \quad (2)$$

where Y represents the predicted response, and β_0 represents the intercept constant. β_i, β_{ii}, and β_{ij} correspond to the linear, quadratic, and interaction regression coefficients, respectively. X_i and X_j are the coded independent variables.

Table 1
Experimental factors and factor levels of the response surface.

Level	Factors		
	A (°C)	B (rpm)	C (h)
−1	50	50	2
0	70	250	4
1	90	450	6

Note: A: temperature, B: stirring rate, C: residence time.

Following the model fitting, analysis of variance was performed to validate the statistical significance and adequacy of the regression model. The fitness was evaluated using the F-value, P-value, and the correlation coefficient (R^2), while the lack-of-fit test ensured that the model accurately represented the data within the experimental range. Subsequently, based on the validated regression equation, 3D response surface plots and contour maps were generated to visually map the response values across the experimental domain and evaluate the interactive effects among variables. Finally, numerical optimization techniques within the software were applied to the polynomial equation to pinpoint the precise optimal crystallization conditions that maximize the particle circularity.

2.5. Characterization

2.5.1. Crystal morphology analysis

Scanning electron microscopy (SEM, TM3000, Hitachi, Japan) was used to analyze the morphology and structure of AFT crystals.

2.5.2. Particle size distribution (PSD)

A particle size analyzer (Mastersizer 3000, Malvern Instruments Ltd., UK) was used to measure the PSD of the AFT product. Pouring the ethanol suspension of AFT into a specific container for analysis. Each sample underwent five measurements, and the average value was recorded as the final result. D_{50} represents the volume average particle diameter.

2.5.3. Online monitoring of AFT crystallization process

In order to investigate the agglomeration mechanism of AFT crystal particles, the experimental procedure was carried out using EasyViewer (400, Mettler Toledo Co. Ltd., Switzerland) technologies. EasyViewer 400, combined with iC Vision analysis software, is a powerful particle size analyzer that can monitor crystallization processes. It can analyze and quantify particle size, particle count, and particle shape through real-time in-situ images (Haer et al., 2021). Furthermore, the system can also continuously measure the chord length distribution (CLD) of particles in intermittent or continuous systems, and then report the distribution and trends in the form of counts per second.

2.5.4. Measurement of AlF_3 concentration in aqueous solution

Due to the exceedingly low aqueous solubility of AlF_3, the concentration of Al^{3+} in the diluted aqueous solution was determined using an Inductively Coupled Plasma-Optical Emission Spectrometer (Agilent 5800 ICP-OES) to infer the overall concentration of AlF_3 in the system.

2.5.5. Circularity

The crystal photos at different experimental conditions were analyzed with a shape analyzer (Occhio Instruments-Callisto 3D 1.7, Belgium), and the circularity data of the crystals at different times were obtained as parameters to characterize the crystal shape. Circularity is a parameter used to describe the similarity of a particle projection to a circle. In general, the higher the sphericity of the particles, the closer the roundness value is to 1. The calculation of the circularity (C) is expressed by (Yu et al., 2021):

$$C = r_1 / r_2 \tag{3}$$

where r_1 is the diameter of a sphere with the same projected area as the particle, and r_2 is the diameter of a circle that is the same as the circumference of the particle projection area.

2.5.6. Flowability

The angle of repose used to assess flowability was determined by the fixed funnel method. Held the funnel vertically above the workbench and poured the samples into the funnel to form a cone until the top of the cone touched the bottom of the funnel. To obtain an accurate result, each sample was measured three times. The angle of repose (θ) using the height (h) of the cone and the radius (r) of the circle, is calculated by (Jitkar et al., 2016):

$$\theta = \tan^{-1}(h / r) \tag{4}$$

2.5.7. Bulk density

Take approximately 50–60 g of the powder sample that has been weighed, then pour it into a glass-graduated cylinder slowly and freely. The top was carefully levelled (avoiding compacting or pressing the powder), and the apparent volume was recorded. To reduce errors, each group of samples was measured three times. The bulk density(ρ_b) could be calculated through the mass (M) and apparent volume (V_0) of the powder sample by (Rausch et al., 2017):

$$\rho_b = M / V_0 \tag{5}$$

2.5.8. Caking ratio

The sample, sieved through a specific mesh sieve, weighed 2.0 g (Model AB204-N, Mettler-Toledo, Switzerland) and was placed in a petri dish. The dish was gently shaken to ensure uniform dispersion of the sample. A certain amount of water was sprayed onto the sample using a spray bottle, followed by drying in an oven at 50 °C for 24 h. Subsequently, the sample was sieved again through the same mesh sieve above. Particles that failed to pass through the sieve tended to cake, and the caking ratio (a) can be estimated from the mass of the agglomerated particles (m) and the total mass of the particles (M) (Zhao et al., 2024):

$$a = m / M \tag{6}$$

3. Results and discussion

3.1. Formation of spherical crystals

To capture agglomeration information of AFT throughout the precipitation process, we carried out crystallization experiments under a constant temperature of 90 °C and a stirring rate of 150 rpm without seeding. The mechanism of AFT spherical crystallization was proposed on the basis of process analysis.

3.1.1. Agglomeration process of AFT

The morphology of AFT crystals sampled at different time intervals was analyzed using SEM. As shown in Fig. 1(a), within approximately 10 min after crystallization began, microcrystals of AFT exhibit short rod-like morphologies with a pronounced propensity for mutual adhesion, forming primary polycrystalline agglomerates. As crystallization proceeds (10-60 min), these crystals adhere to form larger agglomerates, while also continuously adsorbing surrounding newborn and broken crystals. Meanwhile, the crystals on the agglomerates continue to grow, with their aspect ratios increasing and gradually embedding into each other. Ultimately, these interactions led to the formation of relatively stable disordered agglomerates (see Supplementary Fig. S1). It should be emphasized that the presence of irregular protrusions and cracks on the surface of agglomerates at 60 min suggests that initially formed small agglomerates not only continue to capture individual AFT crystals but also coalesce with other small agglomerates.

In parallel, changes in the particle size distribution (PSD) during crystallization are monitored using a Malvern particle size analyzer. As illustrated in Fig. 1(b), during the early stage before 60 min, the particle size of AFT increases rapidly from about 20 μm to around 120 μm, accompanied by a broadening of the size distribution, demonstrating that agglomeration is the dominant mechanism for size increase in the early stage. Fig. 1(c) further shows that D_{10}, D_{50}, and D_{90} all increase significantly over time before 60 min, reinforcing the predominance of the agglomeration mechanism in the initial period.

It is worth noting that the average particle size begins to decrease after 60 min, accompanied by a narrowing of the particle size

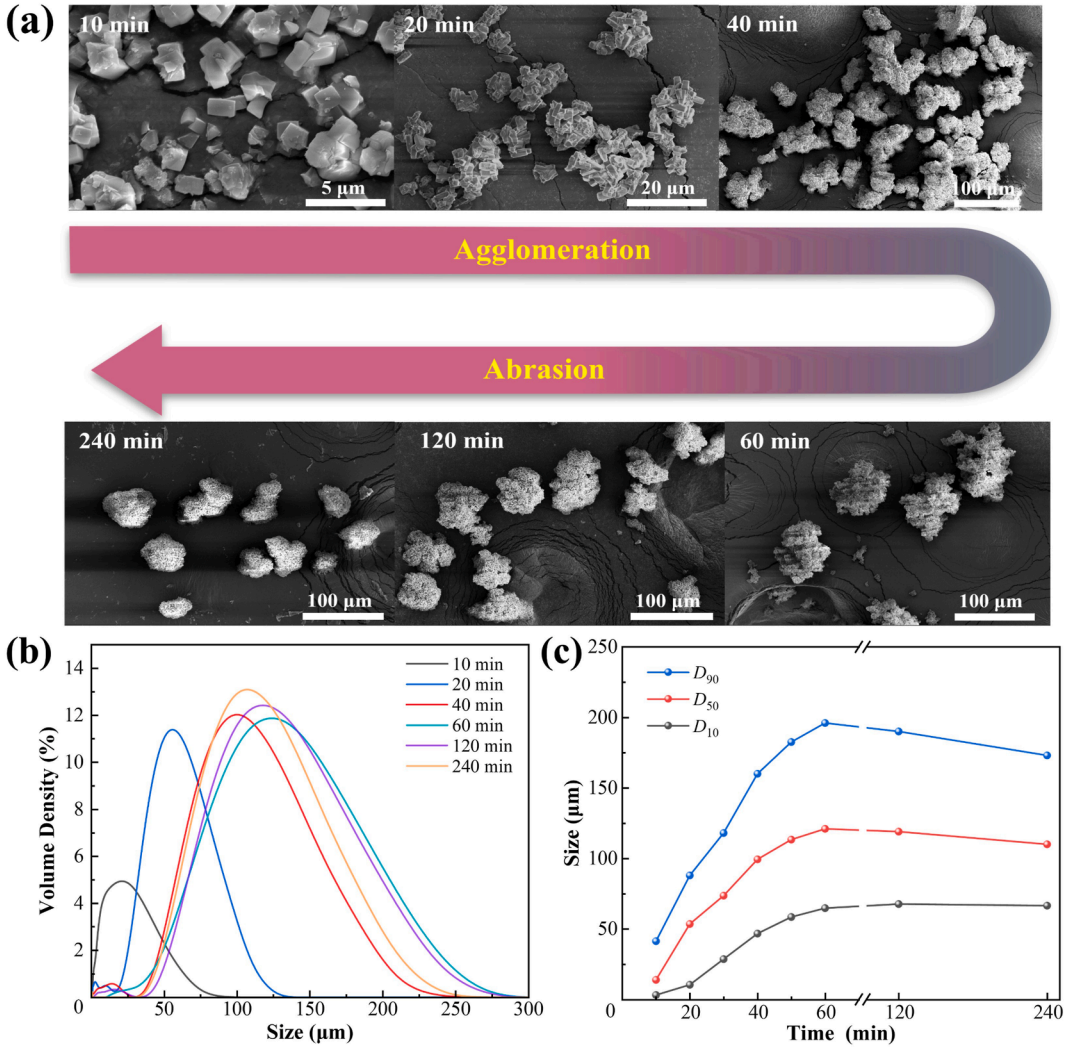

Fig. 1. Time-resolved evolution of AFT spherical particle formation: (a) time-resolved SEM images of AFT spherical evolution process and (b) corresponding changes of particle size distribution; (c) particle size (D_{10}, D_{50}, D_{90}) variation curves over time.

distribution (Fig. 1(b, c)), suggesting that beyond 60 min, the mechanism of mechanical abrasion begins to dominate over agglomeration. However, the significant downward trend of D_{90} indicates that the fragmentation of larger particles likely occurs in the system alongside surface abrasion. As noted above, structurally loose and oversized agglomerates form during the initial rapid agglomeration stage. Under moderate fluid shear stress, these oversized agglomerates inevitably undergo mild breakage into medium-sized secondary agglomerates. As shown in Fig. 1(b), the low proportion of the fine-particle peak at 240 min indicates that the degree of fragmentation during this process is relatively low. The corresponding images (Fig. 1(a)) clearly illustrate the morphological evolution of the particles during this stage (60–240 min). Through continuous breakage and surface abrasion, the initially irregular and loose agglomerates are progressively reshaped into spherical particles.

To capture real-time dynamic information during AFT crystallization, the same system is monitored using an EasyViewer 400 system. Fig. 2(a) presents images of crystal morphology at different times, visually documenting the evolution from initial microcrystals to agglomerates and finally to near-spherical structures, which aligns consistently with the offline SEM observations.

Further insights are gained from the average chord length variation and particle count changes recorded by the EasyViewer. As shown in Fig. 2(c), within the first 10 min of crystallization, the number of fine crystals (1–10 μm) increases sharply, indicating the rapid occurrence of nucleation. Subsequently, the count of small particles decreases rapidly while the proportion of larger particles (10–1000 μm) increases. This shift, accompanied by a continuous decline in the total particle count, indicates that vigorous agglomeration occurs in the early stages. This intense agglomeration is attributed to strong cohesive forces between particles and high collision frequencies resulting from the increasing suspension density. Overall, these findings confirm that the initial rapid growth of AFT particles is primarily driven by agglomeration. After approximately 60 min, particle counts across different size ranges stabilize, indicating that the agglomeration process has reached a limiting state and a dynamic equilibrium is gradually established between agglomeration and the dispersive action induced by stirring. Furthermore, Fig. 2(c) also reveals that, particularly after 80 min, the particle counts within the 10-100 μm size range (blue line) exhibit a gradual upward trend, which precisely corresponds to the medium-sized agglomerates generated from the moderate breakage of the aforementioned oversized agglomerates (>100 μm). It is worth emphasizing that the extremely gradual increase in particle counts within this size range indicates that the fragmentation effect at this stage is relatively mild. Such breakage is limited to a fraction of structurally loose agglomerates, while the morphological reshaping of the entire system remains dominated by the surface abrasion. Likewise, the evolution of the average chord length (Fig. 2(b)) aligns well with the particle size changes in

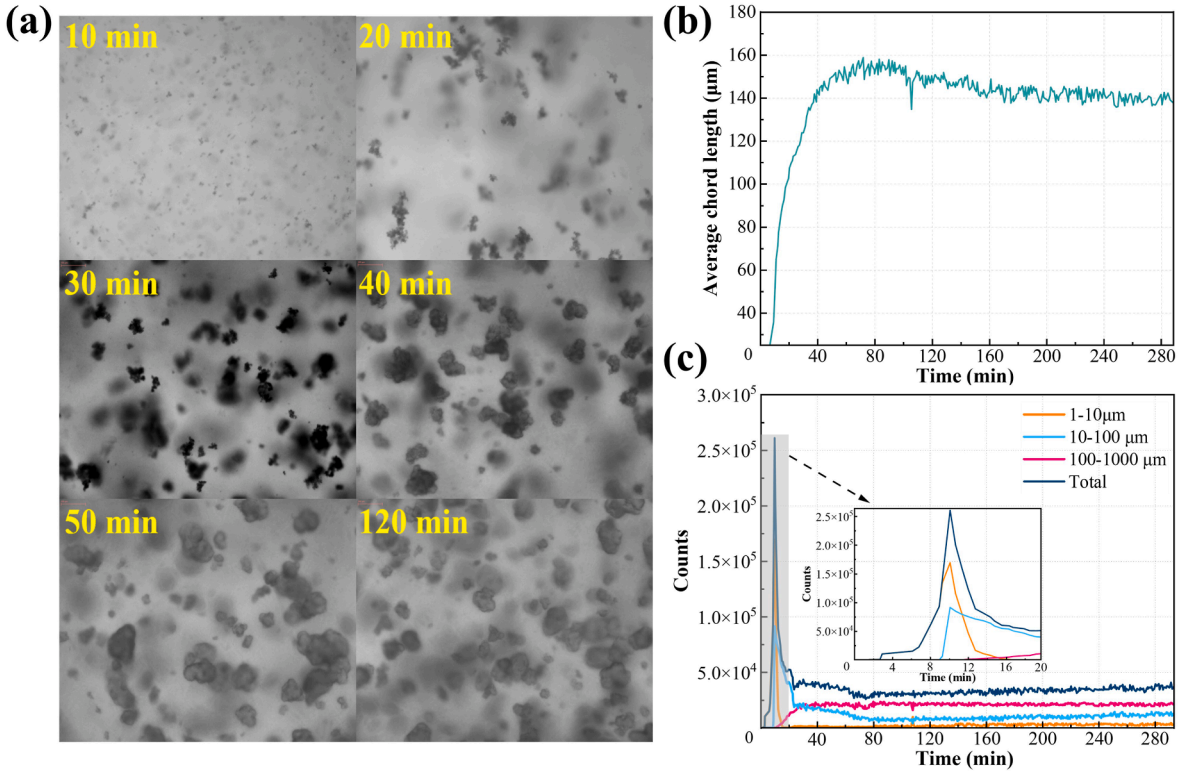

Fig. 2. In-situ observation of AFT precipitation process: (a) crystal morphology monitored by EasyViewer 400; (b) average chord length and particle counts detected by EasyViewer 400.

Fig. 1(c). This further verifies that the AFT crystallization process comprises two primary phases: an initial agglomeration phase (indicated by a rapid increase in chord length) and a subsequent abrasion phase (indicated by a slow decrease in chord length).

The dynamic data of particle count and chord length obtained from online monitoring corroborate the trends of particle size growth and morphological evolution observed offline, collectively establishing the foundation for constructing the agglomeration-abrasion mechanism of AFT spheronization.

3.1.2. *Mechanism of AFT spherical crystallization*

Based on experimental studies of the AFT crystallization process and in combination with previously proposed technologies (Feng et al., 2022; Jin et al., 2018), an agglomeration-abrasion mechanism is

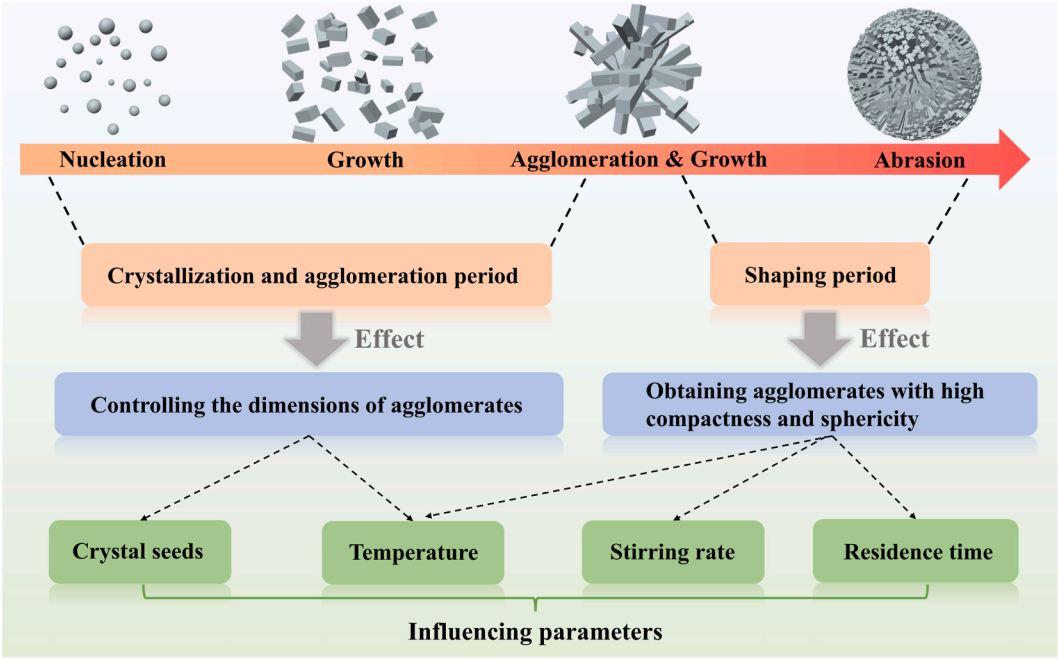

Fig. 3. Scheme of agglomeration-abrasion mechanism.

proposed (Fig. 3). The mechanism involves crystallization (nucleation and growth), agglomeration, and shaping periods. Among them, agglomeration is the key to controlling the particle size and compactness of agglomerates, while shaping is essential to improving the circularity of particles.

During the crystallization stage, the highly supersaturated solution of AFT obtained after the reaction provides a favorable environment for the nucleation and growth of crystals. This stage is controlled by designing the crystallization temperature and crystal seeds, thereby yielding a slurry with high suspended solid density. In the agglomeration period, particles tend to adhere to one another and form agglomerates, leading to a noticeable increase in particle size. Meanwhile, agitation exerts a breaking effect on the agglomerates, and thus the ultimate size of the agglomerates is constrained to an equilibrium between adhesion and hydrodynamic fragmentation, which is primarily governed by the stirring speed. During the subsequent shaping period stage dominated by mechanical wear, the collision and abrasion between the impeller and particles are combined with the gradual growth and interlocking of crystals within and on the surface of the agglomerates. These synergistic effects progressively lead to the formation of spherical particles characterized by smooth surfaces, high sphericity, and compact structure. It is worth mentioning that as the agglomeration of AFT proceeds spontaneously in solution without the requirement for organic reagents, the spherical particle preparation based on this mechanism proves to be more environmentally friendly and efficient.

3.2. Effect of process parameters

To achieve high-performance and high-yield products that meet industrial production requirements, we investigated the effects of seeding, temperature, stirring rate, and residence time on the circularity and yield of AFT crystallization.

3.2.1. Crystal seeding

Fig. 4(a) presents the AlF_3 concentration profiles in both unseeded (Run 1) and seeded (Run 3) solutions at a fixed stirring rate of 150 rpm and crystallization temperature of 90 °C. The slow decline in solute concentration during the initial stage in Run 1 can be attributed to the primary homogeneous nucleation process of AFT in the system. During this period, some crystal nuclei with their limited total surface area slowly consume the supersaturation of the solute. In contrast, the introduction of crystal seeds (Run 3) effectively circumvents stochastic primary nucleation, resulting in a rapid decrease in concentration from the beginning. By providing rough interfaces, the seeds create more nucleation sites and induce sustained, controllable secondary nucleation (Svanberg et al., 2011). This process continuously supplies a large number of microcrystalline units for the agglomeration process and significantly accelerates the consumption rate of supersaturation.

Besides, the seeded crystallization continuously supplies uniformly-sized microcrystalline units for the agglomeration process, thereby significantly enhancing both the agglomeration efficiency and morphological shaping effectiveness of the crystallization process. The evolution of crystal morphology in Run 3 is characterized from the beginning by the presence of numerous, relatively uniform crystal fragments (Fig. S2). Ultimately, the particles obtained exhibit higher circularity, a narrower and uniform distribution compared to that in Run 1 (Fig. 4(b)), and the comparison of particle morphology in the two cases is also shown in Fig. S3.

Furthermore, investigation on the dependence of product circularity and yield on seeded size reveals minimal variation with the alteration of seed size, illustrating a lack of significant correlation between these properties (Fig. 4(c, d)). It demonstrates that seed size is not a critical factor in this agglomeration system, whose influence is likely overshadowed by other parameters such as temperature, stirring rate, and residence time, which may collectively govern the processes of particle

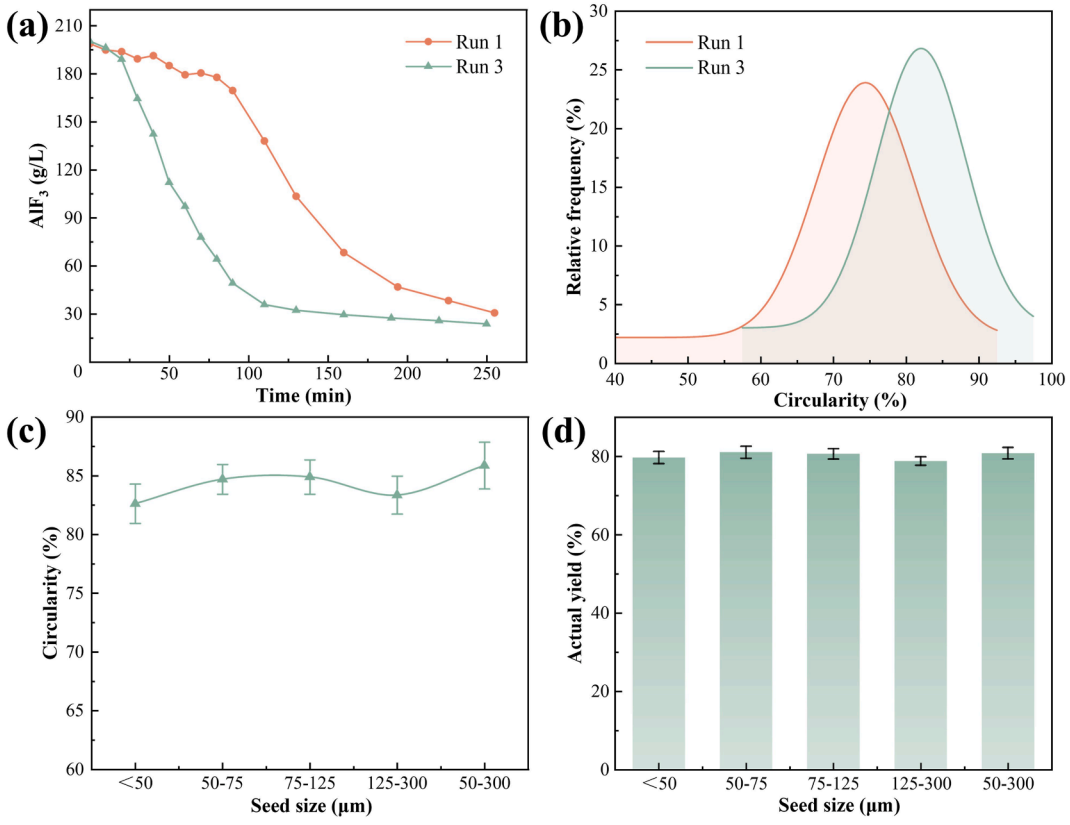

Fig. 4. Effect of crystal seeds on AFT crystallization processes: (a) the concentration depletion profile of AlF3, (b) circularity distribution of AFT products, and the influence of seeded particle size on circularity (c) and actual yield (d).

collision-agglomeration, morphological shaping, and densification.

3.2.2. Temperature

As shown in Fig. 5, both the circularity and actual yield of the product exhibit a strong temperature dependence. The product yield increases significantly with rising temperature, while the circularity also improves noticeably. XRD patterns of AFT products at different temperatures remain almost identical (Fig. S4), which indicates that the anomalous increase in AFT product yield with rising temperature is not caused by solubility differences due to phase transitions. To investigate the thermodynamic factors influencing the crystallization of AFT and explain the increase in yield, we also determined the solubility of AlF_3 at different temperatures using the static method (Issa et al., 2020), as shown in Fig. S5. It should be noted that since the pH of the batch crystallization is consistently maintained at 1.5, the solubility data were also obtained under pH = 1.5 (adjusted with fluorosilicic acid). The solubility of AlF_3 increased only slightly with rising temperature (Fig. S5). By combining that with the initial AlF_3 concentration in the crystallization system (Figs. 4(a), 200 g/L), the theoretical yield at thermodynamic equilibrium for each temperature is estimated, as presented in Fig. 5(b). The theoretical yield, constrained by the very low solubility and weak temperature dependence of AlF_3, changed only minimally and decreased slightly with temperature. In sharp contrast, the actual yield demonstrates a significantly different trend, which suggests that the kinetics governed by temperature—rather than thermodynamic equilibrium—play a decisive role in determining the final product yield and morphology within the limited residence time.

Although lower temperatures offer a higher theoretical yield limit due to reduced equilibrium solubility, the slow kinetics under such conditions prevent the system from approaching equilibrium within the constrained residence time. As corroborated by the AlF_3 concentration profiles at different temperatures during crystallization (Fig. S6), crystallization is delayed at lower temperatures. The system exhibits an induction period of about 40 min at 50 °C before the concentration drops. This suggests that AFT nucleation might be rate-determined by the dehydration barrier of stable $[Al(H_2O)_6]^{3+}$ complexes (Mahmoud & Abbas, 2005), a kinetic limitation similarly observed in other sparingly soluble inorganic salts (Piana et al., 2006). As a result, a significant amount of solute remains in the solution, leading to a lower actual yield. In contrast, although higher temperatures slightly increase the equilibrium solubility of AFT, the abundant thermal energy readily overcomes this dehydration barrier. Consequently, they substantially accelerate the rate of mass transfer and crystallization, leading to rapid consumption of supersaturation and thus a higher yield within the given timeframe. As shown in Fig. 5(b), on the one hand, an actual average product yield of 80.82% is achieved over 4 h at 90 °C, representing an approximately threefold enhancement compared to the yield obtained at 50 °C.

On the other hand, a higher temperature markedly enhances nucleation and growth rate of AFT, as well as the suspension density of particles in the solution. Meanwhile, it also reduces the solution viscosity, thereby further increasing the frequency of effective collisions of crystals. Moreover, the high rate of molecular diffusion caused by high temperature facilitates the rapid formation of crystal bridges (Jin et al., 2018) between initially adhered particles and thereby stabilizes the agglomerates against disruption by agitation. As a result, these agglomerates, with their high mechanical strength, maintain structural stability in solution even during the high-shear shaping stage and develop rapidly towards highly dense spherical structures, thereby enhancing spheroidization efficiency. It is worth emphasizing that the crystallization temperature is optimized up to 90 °C, which is established as the upper limit for this study. While temperatures above 90 °C could further improve sphericity possibly, they are deemed unsuitable for scalable operation. The risks of solution boiling and alteration in solution composition at elevated temperatures pose significant challenges to process control and product consistency, thus making 90 °C a prudent upper limit for industrial translation.

3.2.3. Stirring rate

Fig. 6(a) shows that the circularity of the particles increases with increasing stirring rate at 90 °C and 4 h. Under the high stirring rate (450 rpm), the circularity of particles even increases to 86.27% while the particle circularity is only 69.06% at the low stirring rate (50 rpm). The shape of crystals is mostly determined by the mechanics of collision and the magnitude of the shear stress (Bosetti & Mazzotti, 2019). The crystals are more or less rounded as a result of attrition, so that the higher the stirring rate, the greater is the degree of attrition. Due to the high shear stress provided by the stirring rate of 450 rpm, the products are all nearly spherical. However, as the stirring rate increases beyond 250 rpm, the fluid shear forces might gradually approach or exceed the mechanical strength of the agglomerates. So excessive fluid shear forces and collision-induced crystal abrasion and fragmentation begin to manifest as detrimental effects, causing the rate of roundness improvement to slow.

The variation in product yield with different stirring rates (Fig. 6(b)) shows that as the stirring rate increases, the average yield rises slightly resulting from alterations in crystallization conditions caused by adjustments to the stirring rate (Yang et al., 2017). By increasing the stirring rate, the collisions among crystals, as well as between the impeller and the crystals, become more frequent and intense, which leads to the fragmentation of existing crystals and encourages the formation of new crystal nuclei. As a result, the available surface area for mass transfer is expanded, which promotes crystal growth and improves the overall efficiency of the crystallization process.

The stirring rate was optimized with an upper limit of 450 rpm,

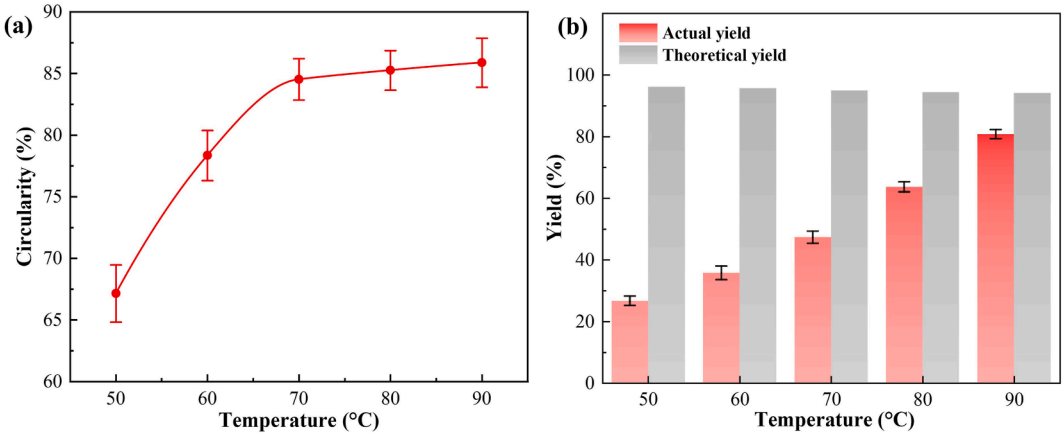

Fig. 5. Effect of crystallization temperatures on the product circularity (a) and actual and theoretical product yields (b).

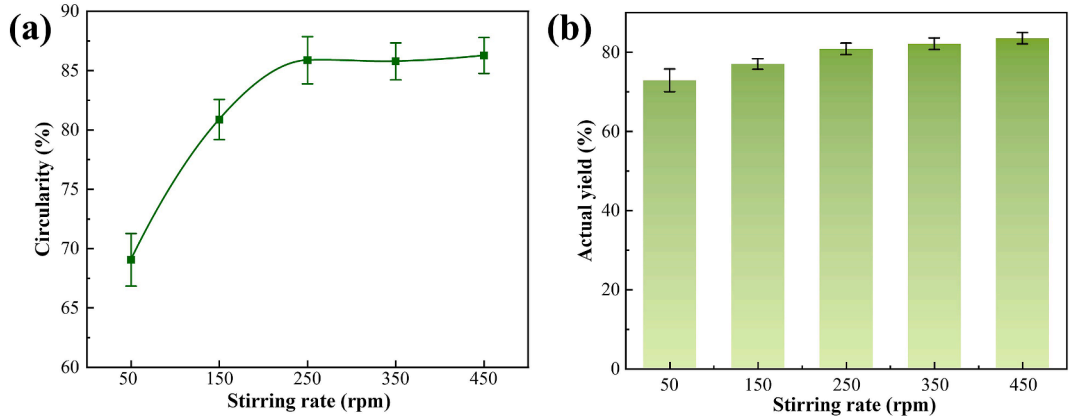

Fig. 6. Effect of stirring rates on the product circularity (a) and actual product yield (b).

which represents the maximum allowable value in this process. Although higher shear forces can theoretically further abrade particle surfaces, exceeding this threshold predominantly induces excessive crystal fragmentation. Extreme fluid shear forces (550 rpm) surpass the mechanical strength of the particles, triggering overall destructive fragmentation. It not only results in a highly non-uniform and severe bimodal particle size distribution (Fig. S7(a)), but also generates a mass of irregular fine crystals and shattered fragments (Fig. S7(b)) that adversely affect product handling. Additionally, excessively high stirring speeds lead to a sharp increase in energy consumption during production. Therefore, 450 rpm is established as the maximum stirring speed in this study to ensure both product quality and relatively low energy consumption.

3.2.4. Residence time

With the increase of residence time, the particle circularity is also continuously improved when the temperature and stirring rate are set at 90 °C and 250 rpm, respectively (Fig. 7(a)). It is mainly due to the shear action of the stirring paddle on the particles and the collision between the particles. When the suspension time reaches 6 h, the particle circularity (86.87%) is close to the maximum value. A sufficiently long suspension time (6 h) ensures crystal growth and embedding, alongside agglomerates abrasion during the shaping period. This prolonged abrasive action results in the gradual removal of surface edges and irregular protrusions and promotes the overall smooth and spheroidization of their contours.

In addition, the slowing growth trend of product circularity after 4 h indicates that the critical shaping period occurs prior to this time. Meanwhile, from the yield trend in Fig. 7(b), it is evident that prior to 4 h, the AFT precipitation rate is relatively rapid. After that, the yield grows slowly due to the continuous decreases in supersaturation and crystallization driving force, which is consistent with the trend in concentration of AlF_3 in Run 3 shown in Fig. 4(a).

3.3. Response surface analysis

Single-factor analysis has preliminarily revealed the individual effects of various parameters on the circularity of the AFT product. However, during the actual crystallization processes, factors such as temperature, stirring rate, and residence time are likely to exhibit complex interactions, collectively governing the dynamic balance between agglomeration and abrasion. Therefore, it is necessary to employ multivariate optimization methods for further investigation.

3.3.1. Model fitting and statistical analysis

Based on the preliminary experimental results, three parameters of temperature (A), stirring rate (B), and residence time (C) are further investigated using response surface analysis to understand their interactive effects on particle circularity and determine the optimal crystallization conditions (Table 1). The design matrix and corresponding experimental results are shown in Table S2, and the Design-Expert software is used for data analysis. The response variable of the particle circularity (Y) can be described by the following second-order polynomial equation:

$$Y = -7.39504 + 1.88850A - 0.01243B - 3.55815C - 8.37 \times 10^{-4}AB + 0.07819AC + 7.66 \times 10^{-3}BC - 0.015240A^2 - 1.5 \times 10^{-4}B^2 - 1.11155C^2$$

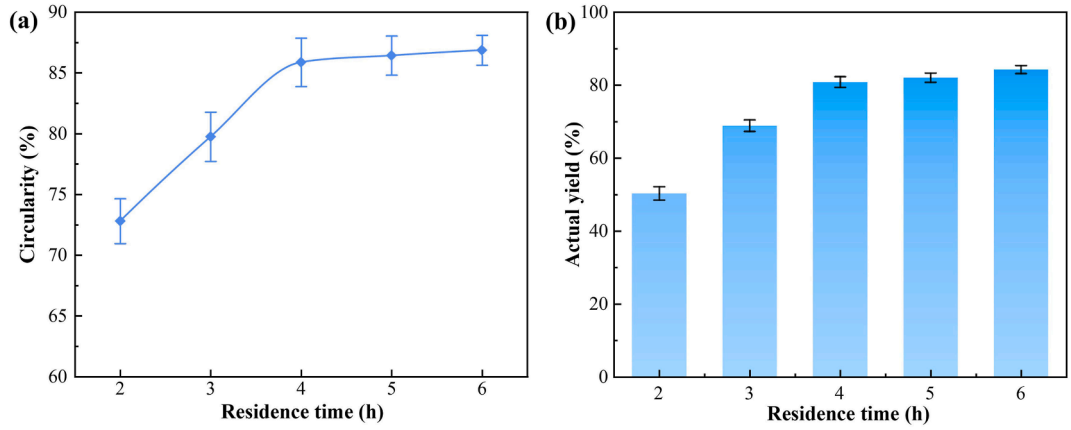

Fig. 7. Effect of residence time on the product circularity (a) and actual product yield (b).

As can be seen from Table 2, F = 72.82 with a P-value <0.0001 indicates that the linear relationship between the dependent variable and three independent variables is good and that the model reaches an extremely significant level. The misfit term of the model is used as a measure of the measurement data that it cannot represent within the experimental range (Huang & Lin, 2024), and the P-value for the misfit term in this experiment is 0.9393 > 0.05, which is insignificant compared to the pure error. Finally, the coefficient of variation of the equation CV = 1.74%, which indicates that the proportion of unexplained total variation is small, and the experimental value is reliable. The coefficient of determination R^2 = 0.9894 and the correction coefficient Adjust R^2 = 0.9758 indicate a great fit between the values predicted by the model and experimental ones. Therefore, the Y regression equation could be used to replace the real point to analyze the experimental results. The F-value and P-value can be used to test the significance of each coefficient and to assess the strength of the interaction between each factor (Sun et al., 2017). According to the P-values and F-values of the factors of the model, the temperature (A), stirring rate (B), and residence time (C) have significant impacts on the circularity of AFT particles (P < 0.05) and the order of influence is A > B > C. Besides, the effects of AB, AC, and BC on circularity are all statistically extremely significant in the interaction term (P < 0.05).

3.3.2. Response surface analysis

The response surface diagram is a three-dimensional surface plot representing the relationship between the factors under investigation and the response value (Sun et al., 2017). The degree of influence of each interaction factor on the response value can be observed by examining the slope of the surface, allowing for the verification of interactions among the variables under investigation (Sun et al., 2017). If the response surface has a steeper slope, and the contours are tight, it indicates that the interaction between the two factors has a significant impact on the response value (Wang et al., 2018). Fig. 8 shows the contour plot and response surface among temperature (A), stirring rate (B), and residence time (C), and each figure illustrates how the interaction of any two factors impacts the response value while holding the third factor at a certain level.

In all sets of response surface plots, the maximum values of the response surface are consistently located at the highest levels of the three factors, which align with the results from the single-factor experiments, indicating synergistic effects among them. Notably, the response surface corresponding to the interaction between A and B (Fig. 8(a)) exhibits the steepest slope, accompanied by the densest contour lines (Fig. 8(b)), suggesting a particularly strong synergistic effect between them. In contrast, although the response surfaces for the interactions between A and C (Fig. 8(c, d)) and between B and C (Fig. 8(e, f)) also show considerable slopes, their steepness is less pronounced than that of the AB interaction. This observation is in well consistent with the proposed agglomeration-abrasion mechanism. An increase in temperature, as the most crucial factor according to Table 2, not only accelerates the kinetics of crystal nucleation, growth, and agglomeration, but more critically, enhances the rates of molecular diffusion, crystal bridging, and embedding. These effects rapidly stabilize the initially formed loose agglomerates, increase mechanical strength and endow them with plasticity. Meanwhile, the stirring rate directly governs the magnitude of shear stress, serving as the primary driving force for surface abrasion essential for spheroidization.

Fundamentally, this strong AB interaction reflects a dynamic balance: the temperature-driven structural stability of the agglomerates must properly match the fluid shear stress. This synergy enables continuous surface abrasion to remove irregularities without causing catastrophic fragmentation. So the interaction of temperature and stirring becomes the most decisive factor for circularity in this system. However, although residence time provides the necessary duration for particle abrasion, the critical spheroidization stage dominated by temperature and stirring rate primarily occurred in the early phase, which leads to a diminished contribution from the prolonged abrasive effect of residence time in the later stages. Consequently, the AB interaction exhibits a more significant effect on circularity compared to the AC and BC, resulting in a steeper response surface.

As shown in Fig. 9, at the fixed residence time of 4 h, the circularity of the products increases with the elevation of two key factors (i.e., crystallization temperature and stirring rate), due to enhanced agglomeration efficiency and shear force. When the temperature and stirring rate reach 90 °C and 450 rpm respectively, the obtained crystals become almost completely spherical shape, which is consistent with the response surface data. It is worth mentioning that the particle size is also larger at high temperatures, which is likely attributed to the crystallization rate and agglomeration efficiency of the crystalline system.

3.4. Product performance and industrial feasibility

Based on the optimization function derived from Design-Expert, the optimal process parameters are determined as a temperature of 90 °C, a stirring speed of 450 rpm, and a residence time of 6 h. The predicted maximum circularity from the model is 92.49%. To validate the reliability of the model, AFT products prepared under these optimal conditions have an average circularity of 90.74% ± 0.5%, which is in well line with the predicted value. To demonstrate the advantages of the product in post-processing and application, the performance of the produced spherical AFT particles was examined and compared with two types of commercial products.

3.4.1. Product properties comparison

The morphology of resultant AFT products is given in Fig. 10(a). These two commercial products, one rod-shaped and the other irregularly lumpy (Fig. 10(a)), are both produced via a conventional fluorination process. These commercial products are evaluated in their as-

Table 2
Variance analysis results of the regression model of circularity.

Source	Sum of squares	Deg. of freedom	Mean square	F-value	P-value	Significant level
Model	1165.64	9	125.52	72.82	<0.0001	Significant
A	246.64	1	246.64	138.68	<0.0001	
B	226.24	1	226.24	127.20	<0.0001	
C	134.87	1	134.87	75.83	<0.0001	
AB	44.88	1	44.88	25.23	0.0015	
AC	39.12	1	39.12	22.00	0.0022	
BC	37.52	1	37.52	21.10	0.0025	
A^2	156.38	1	156.38	87.92	<0.0001	
B^2	151.92	1	151.92	85.42	<0.0001	
C^2	83.24	1	83.24	46.80	0.0002	
Residual error	12.45	7	1.78			
Lack of fit	1.08	3	0.36	0.13	0.9393	No significant
Pure error	11.37	4	2.84			
Cor total	1178.09	16				

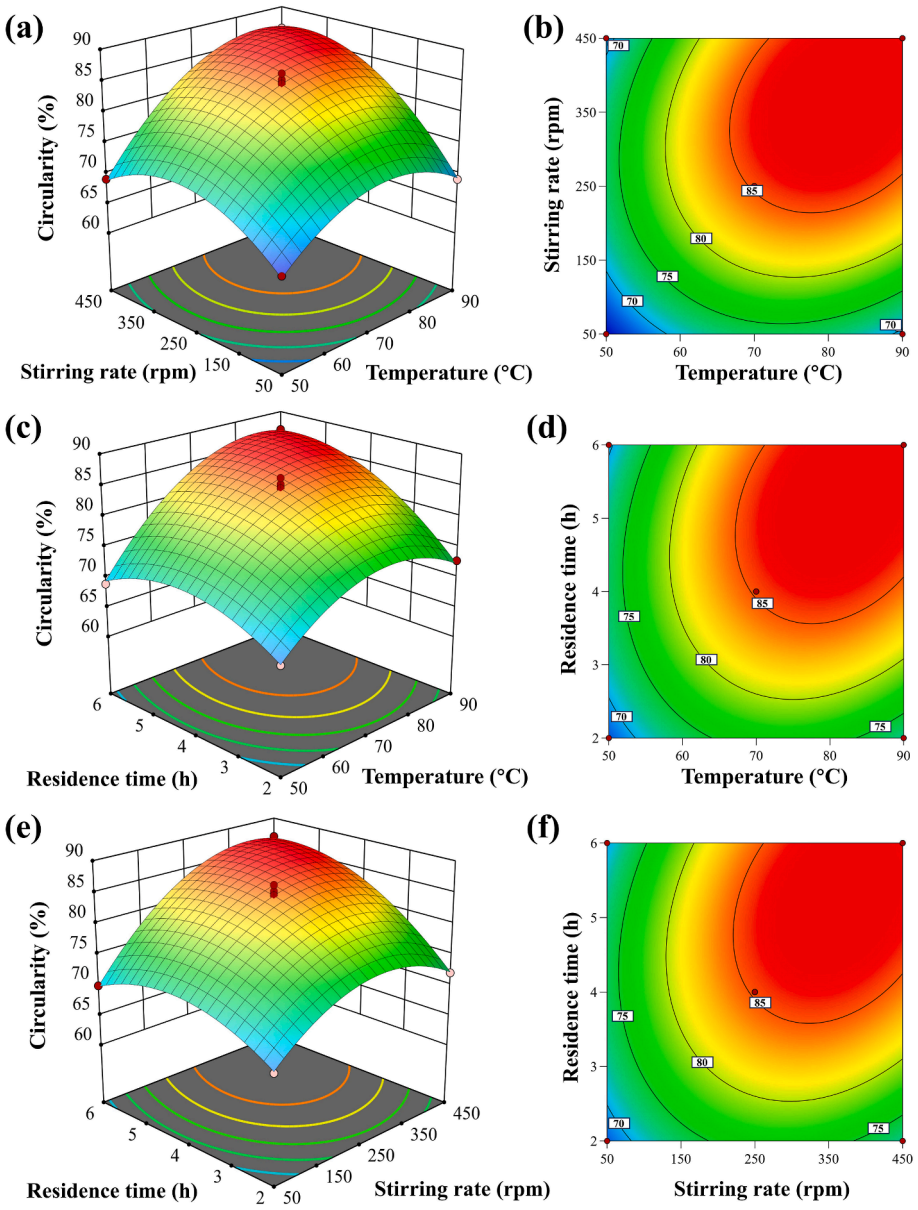

Fig. 8. Response surfaces and contour plots of the interaction of the experimental factors: the interaction between (a, b) temperature and stirring rate; (c, d) temperature and residence time; (e, f) stirring rate and residence time.

synthesized states without any post-treatment. Commercial product 1 is synthesized through the traditional hydrofluoric acid route. This process involves reacting $Al(OH)_3$ with HF followed by high-temperature evaporative crystallization (Chen et al., 2021), where sustained high supersaturation promotes anisotropic growth to yield rod-like crystals. And commercial product 2 derives from a conventional unseeded batch crystallization process typically conducted at approximately 75 °C with low agitation. These moderate conditions aim to minimize initial energy inputs, prioritizing basic mass recovery over crystal morphology regulation. However, the absence of seed crystals triggers uncontrolled primary nucleation (Nielsen & Altintas, 1984). Combined with insufficient fluid shear to disperse the massive fine nuclei, this environment allows for prolonged random particle cementation, inevitably yielding disordered and irregular lumps.

A repose angle below 30° indicates good flowability, while a value above 30° suggests poor flowability (Jin et al., 2018). As shown in Fig. 10(b), the spherical AFT crystals prepared via the agglomeration–abrasion strategy exhibit the lowest angle of repose (19.3°), representing reductions of 41.4% and 24.5% compared to the two commercial counterparts, respectively. It can be attributed to the smooth surface and low interparticle friction of the spherical crystals, which endow the material with excellent powder flowability. This property significantly enhances material transport efficiency from production to end-use applications, while avoiding issues such as pipeline clogging, scaling during processing, and electrostatic charging of the powder. Besides, the bulk density, which represents the mass per unit volume of powder in a naturally settled state, reaches a maximum value of 0.904 g/mL, representing increases of 30.1% and 22.5% compared to the two commercial powders. This high bulk density improves spatial utilization, reduces storage costs, and substantially mitigates dust-related risks.

The anti-caking ability of the AFT products is assessed using the caking ratio. Fig. 10(c) compares the caking ratios of spherical AFT products with two commercial powders in the presence of various amounts of water. The caking ratios of both spherical products and commercial powders increase with an increase in water spraying. Nevertheless, the caking ratio of the spherical products remains significantly lower than that of the raw material. Under varying amounts of

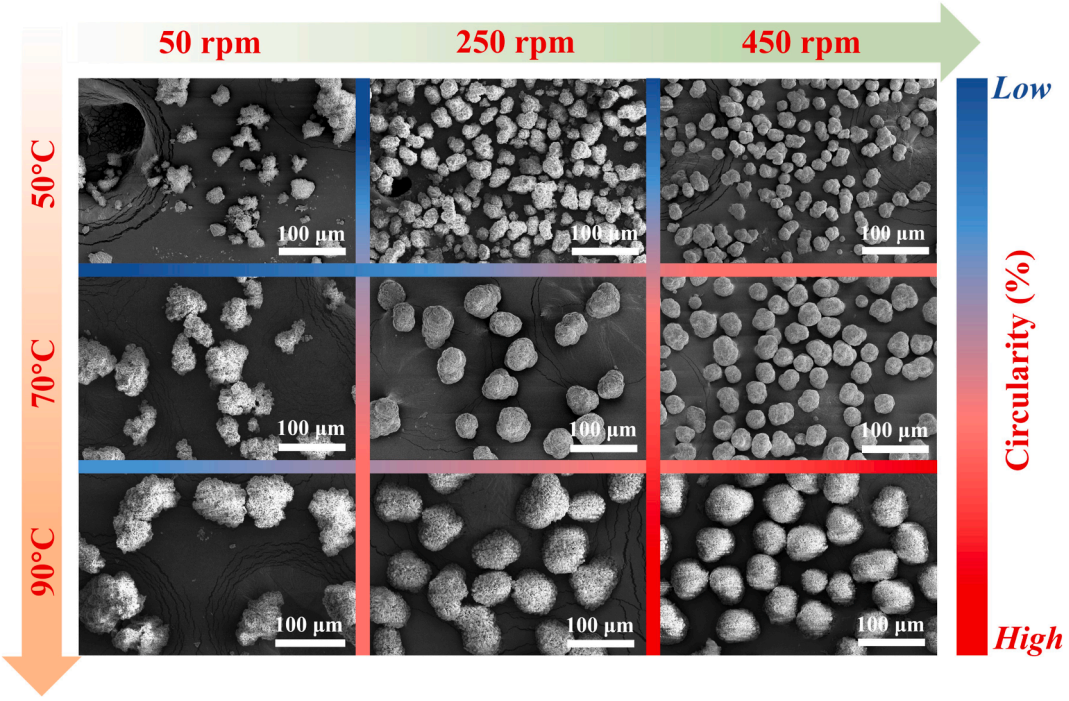

Fig. 9. Synergistic effects of crystallization temperature and stirring rate on the morphology evolution of AFT spherical particle formation.

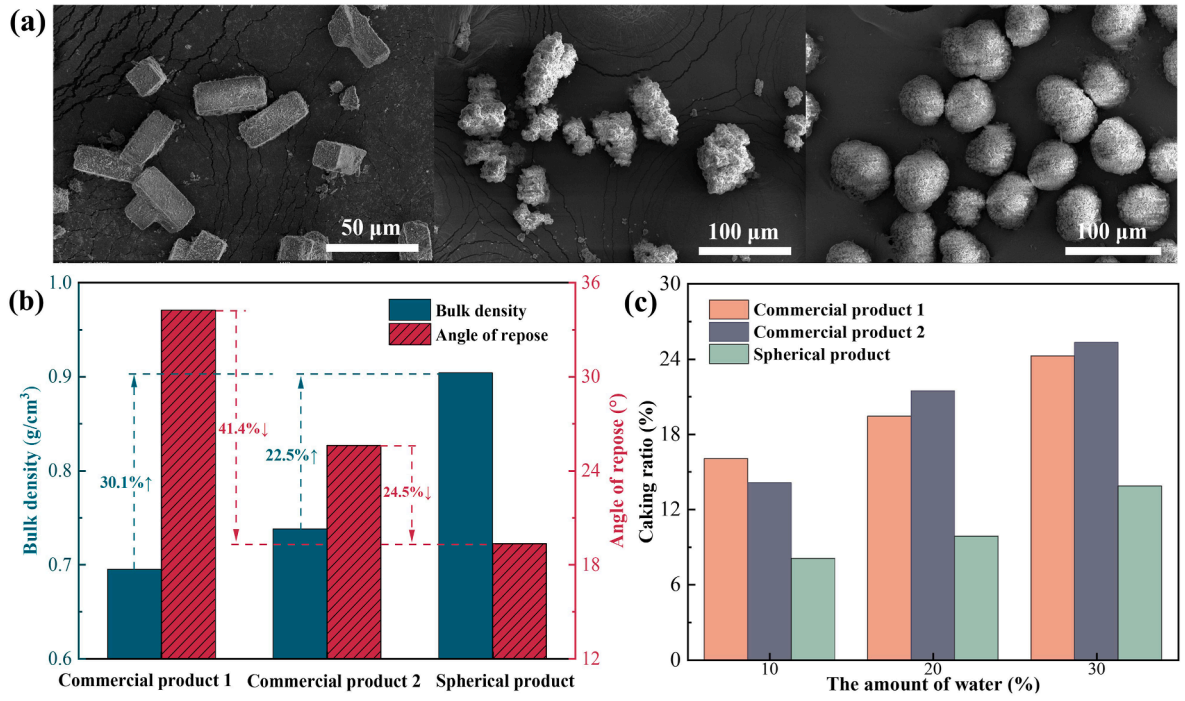

Fig. 10. Characterization of commercial and spherical product produced in this work: (a) the morphology of commercial product 1 (left), commercial product 2 (middle), spherical product (right); (b, c) comparisons of bulk density and angle of repose (b) and caking ratio (c).

water, the average caking ratios of the spherical products decreased by approximately 47.2% and 46.8% compared to commercial products 1 and 2, respectively. This difference can be primarily attributed to the influence of crystal morphology on moisture removal efficiency (Thakur et al., 2016). The irregular crystals, due to their larger interparticle contact area and complex pore structure, tend to retain moisture. In contrast, the spherical particles, benefiting from their regular geometry and point-contact characteristics, effectively minimize the moisture retention. Benefiting from an exceptionally low caking ratio, the optimized spherical AFT particles eliminate the need for additional crushing equipment during transportation and storage. Simultaneously, their reduced moisture content significantly lowers thermal energy consumption in the subsequent calcination process for producing AlF_3. Moreover, to exclude the influence of particle size, the three products were sieved to identical sizes for further evaluation (Fig. S8(a)). Notably, the spherical AFT still exhibits significantly superior bulk

density, flowability, and anti-caking performance compared to the commercial references (Fig. S8(b–c)). This verifies that spherical morphology is the key factor in enhancing powder properties.

3.4.2. Production yield and industrial feasibility

Under optimal conditions, the actual yield of AFT reached 85.7%. Compared with the theoretical limit yield of ~94% (based on solubility data in Fig. S5), the process achieves a high degree of supersaturation consumption within a reasonable residence time. This high yield not only maximizes the utilization of raw materials but also significantly reduces the solute content in the mother liquor, thereby lowering the cost and environmental burden of wastewater treatment. Compared to conventional crystallization at lower temperatures and stirring rates (~60% yield), this strategy increases the batch capacity by approximately 25 percentage points, demonstrating economic viability for industrial scale-up.

Although optimized conditions increase crystallization temperatures and stirring intensity, leading to higher thermal and mechanical energy consumption, the significant improvement in batch yield is expected to compensate for this additional energy input. Beyond yield benefits, the spherical product's excellent flowability saves downstream handling costs (e.g., eliminating extra crushing or pipeline clogging) and paves the way for continuous production processes for AFT, enabling further capacity expansion. Coupled with reduced hygroscopicity, these spherical particles substantially decrease the thermal load during subsequent calcination to produce AlF_3. The synergistic optimization of yield and morphology represents a key step toward a more energy-efficient and cost-effective large-scale production process.

4. Conclusion

In summary, we have successfully developed an environmentally friendly, additive-free "agglomeration–abrasion" strategy to directly crystallize high-performance spherical AFT particles in an aqueous solution. By integrating offline characterizations with online in-situ monitoring, this study reveals a novel spherical agglomeration mechanism of AFT. Specifically, the transition from primary microcrystals to dense spherical agglomerates is governed by a dynamic synergy: temperature drives rapid agglomeration and structural consolidation, while stirring provides the essential mechanical abrasion. Based on single-factor analysis, we employed response surface methodology to quantify the interactive effects among these key parameters and identify the optimal conditions as 90 °C, 450 rpm, and 6 h. Under these optimal conditions, the prepared AFT particles achieved an excellent average circularity of 90.74% alongside a high actual yield of 85.7%. Compared to the findings of other workers who rely on complex solvent systems or organic bridging liquids for spherical crystallization, this strategy successfully prepares highly spherical particles without introducing additional processing complexities. Furthermore, in contrast to commercial irregular AFT products, the optimized spheres successfully overcome inherent flow resistance and caking issues, delivering maximum improvements of 30.1% in bulk density and 41.4% in flowability. Overall, the AFT prepared in this study features both high yield and superior powder properties, effectively resolving current production bottlenecks and demonstrating significant potential for continuous industrial manufacturing. More importantly, the proposed strategy and research methodology provide a practical approach for spherical crystallization of other inorganic salts.

CRediT authorship contribution statement

Shubo Liu: Writing – review & editing, Writing – original draft, Validation, Methodology, Investigation, Formal analysis, Conceptualization. **Jiantao Yan:** Writing – review & editing, Validation, Methodology, Investigation, Conceptualization. **Shengzhe Jia:** Writing – review & editing, Investigation, Conceptualization. **Ke Yu:** Writing – review & editing, Validation, Conceptualization. **Huamin Yin:** Validation, Investigation. **Shulin Chen:** Validation, Methodology, Investigation. **Weiwei Tang:** Writing – review & editing, Writing – original draft, Supervision, Resources, Project administration, Conceptualization. **Junbo Gong:** Writing – review & editing, Writing – original draft, Resources, Funding acquisition, Conceptualization.

Declaration of competing interest

The authors declare that they have no known competing financial interests or personal relationships that could have appeared to influence the work reported in this paper.

Acknowledgments

The authors are grateful for the financial support of the National Natural Science Foundation of China (grant Nos. NSFC 22278300 and 22478284) and the Natural Science Foundation of Tianjin (grant No. 22JCZDJC00040).

Appendix A. Supplementary data

Supplementary data to this article can be found online at https://doi.org/10.1016/j.partic.2026.04.025.

References

Bezerra, M. A., Santelli, R. E., Oliveira, E. P., Villar, L. S., & Escaleira, L. A. (2008). Response surface methodology (RSM) as a tool for optimization in analytical chemistry. *Talanta, 76*, 965–977. https://doi.org/10.1016/j.talanta.2008.05.019

Bosetti, L., & Mazzotti, M. (2019). Population balance modeling of growth and secondary nucleation by attrition and ripening. *Crystal Growth & Design, 20*, 307–319. https://doi.org/10.1021/acs.cgd.9b01240

Carpin, M., Bertelsen, H., Dalberg, A., Bech, J. K., Risbo, J., Schuck, P., & Jeantet, R. (2017). How does particle size influence caking in lactose powder? *Journal of Food Engineering, 209*, 61–67. https://doi.org/10.1016/j.jfoodeng.2017.04.006

Chen, G., Yang, X., Qu, J., Luo, J., Zhang, Z., & Sun, L. (2021). Kinetic study on the preparation of aluminum fluoride based on fluosilicic acid. *Polish Journal of Chemical Technology, 23*, 10–16. https://doi.org/10.2478/pjct-2021-0024

Feng, S., Yao, M., Guo, S., Lin, J., Ao, Z., Yu, C., Li, K., Xun, C., Yang, L., He, J., et al. (2022). Morphology and microstructure regulation of inorganic salts in an additive-free water system via the self-organization of hierarchical crystal clusters: Mechanism, model, and applications. *Chemical Engineering Science, 262*, Article 118053. https://doi.org/10.1016/j.ces.2022.118053

Feng, S., Yu, C., Guo, S., Ouyang, J., Yin, F., Zhang, X., Zhang, Y., Chen, M., Han, D., Gong, J., & Wang, J. (2023). Design spherical particles of potassium peroxymonosulfate compound salt with high stability and good powder properties via an agglomeration-dissolution mechanism. *Particuology, 80*, 157–169. https://doi.org/10.1016/j.partic.2022.11.020

Ferreira, S. L. C., Bruns, R. E., Ferreira, H. S., Matos, G. D., David, J. M., Brandão, G. C., da Silva, E. G. P., Portugal, L. A., dos Reis, P. S., Souza, A. S., & dos Santos, W. N. L. (2007). Box-Behnken design: An alternative for the optimization of analytical methods. *Analytica Chimica Acta, 597*, 179–186. https://doi.org/10.1016/j.aca.2007.07.011

Haer, M., Strahlendorf, K., Payne, J., Jung, R., Xiao, E., Mirabel, C., Rahman, N., Kowal, P., Gemmiti, G., Cronin, J. T., Gable, T., Park-Lee, K., Drolet-Vivies, K., Balmer, M., & Kirkitadze, M. (2021). PAT solutions to monitor adsorption of Tetanus Toxoid with aluminum adjuvants. *Journal of Pharmaceutical and Biomedical Analysis, 198*, Article 114013. https://doi.org/10.1016/j.jpba.2021.114013

Hou, J., Shi, D., Wang, Z., Gao, B., Shi, Z., & Hu, X. (2017). Influence of additives on Bath analysis in aluminum electrolysis. *JOM, 69*, 2057–2064. https://doi.org/10.1007/s11837-017-2482-8

Huang, G., & Lin, B. (2024). Preparation for shaddock skin polysaccharide derivatives by response surface method. *Scientific Reports, 14*, Article 14054. https://doi.org/10.1038/s41598-024-63851-w

Issa, Y. M., Abdel-Fattah, H. M., & Mohamed, N. B. (2020). Solubility and thermodynamic studies of sparingly soluble tellurite salts. *Journal of Thermal Analysis and Calorimetry, 145*, 3207–3217. https://doi.org/10.1007/s10973-020-09932-0

Jin, S., Chen, M., Li, Z., Wu, S., Du, S., Xu, S., Rohani, S., & Gong, J. (2018). Design and mechanism of the formation of spherical KCl particles using cooling crystallization without additives. *Powder Technology, 329*, 455–462. https://doi.org/10.1016/j.powtec.2018.02.001

Jitkar, S., Thipparaboina, R., Chavan, R. B., & Shastri, N. R. (2016). Spherical agglomeration of platy crystals: Curious case of etodolac. *Crystal Growth & Design, 16*, 4034–4042. https://doi.org/10.1021/acs.cgd.6b00563

Kubiňáková, E., Danielik, V., & Híveš, J. (2018). Electrochemical characterization of multicomponent sodium cryolite electrolytes with high content of aluminium

fluoride. *Electrochimica Acta, 265*, 474–479. https://doi.org/10.1016/j.electacta.2018.01.17

Lai, F., Sun, Z., Saji, S. E., He, Y., Yu, X., Zhao, H., Guo, H., & Yin, Z. (2021). Machine learning-aided crystal facet rational design with ionic liquid controllable synthesis. *Small, 17*, Article 2100024. https://doi.org/10.1002/smll.202100024

Li, J., Gao, Y., Wang, J., Niu, L., Ge, Y., Zhang, Y., Chen, M., & Gong, J. (2024). Preparation of $(NH_4)_2SO_4$ spherical particles with functions of sustained-release and anticaking by an organic solvent-free process. *Industrial & Engineering Chemistry Research, 63*, 18212–18220. https://doi.org/10.1021/acs.iecr.4c02589

Long, B., Wang, Z., Zhang, Q., Ke, W., & Ding, Y. (2018). Improved process to prepare high-purity anhydrous potassium fluoride from wet process phosphoric acid. *Chemical Engineering Communications, 205*, 1342–1350. https://doi.org/10.1080/00986445.2018.1450246

Mahmoud, B., & Abbas, T. (2005). Investigation of different stages of aluminum fluoride crystal growth. *Iranian Journal of Chemistry and Chemical Engineering, 24*, 27–32. https://sid.ir/paper/539888/en.

Nielsen, A. E., & Altintas, N. D. (1984). Growth and dissolution kinetics of aluminium fluoride trihydrate crystals. *Journal of Crystal Growth, 69*, 213–230. https://doi.org/10.1016/0022-0248(84)90326-9

Passerini, N., Calogerà, G., Albertini, B., & Rodriguez, L. (2010). Melt granulation of pharmaceutical powders: A comparison of high-shear mixer and fluidised bed processes. *International Journal of Pharmaceutics, 391*, 177–186. https://doi.org/10.1016/j.ijpharm.2010.03.013

Piana, S., Jones, F., & Gale, J. D. (2006). Assisted desolvation as a key kinetic step for crystal growth. *Journal of the American Chemical Society, 128*, 13568–13574. https://doi.org/10.1021/ja064706q

Rausch, A., Küng, V., Pobel, C., Markl, M., & Körner, C. (2017). Predictive simulation of process windows for powder bed fusion additive manufacturing: Influence of the powder bulk density. *Materials, 10*, 1117. https://doi.org/10.3390/ma10101117

Shinde, G. S., & Mohite, S. (2020). Improvement in bioavailability of oxcarbazepine using spherical agglomeration. *International Journal of Pharmaceutical Sciences and Research, 11*, 2118–2126. https://doi.org/10.13040/IJPSR.0975-8232.11(5).2118-26

Stirk, A. J., Souza, F. E. S., Gerster, J., Mir, F. M., Karadeolian, A., & Rey, A. W. (2022). Formation of pharmaceutical salts and cocrystals via vapour-assisted tumbling (VAT) – A solvent efficient process. *Green Chemistry, 24*, 1505–1514. https://doi.org/10.1039/D1GC03683A

Sun, X., Kim, S., Yang, S. D., Kim, H. S., & Yoon, J. Y. (2017). Multi-objective optimization of a stairmand cyclone separator using response surface methodology and computational fluid dynamics. *Powder Technology, 320*, 51–65. https://doi.org/10.1016/j.powtec.2017.06.065

Sun, M., Liu, Y., Yan, H., Chen, M., & Gong, J. (2021). Highly-efficient production of spherical co-agglomerates of drugs via an organic solvent-free process and a mechanism study. *Green Chemistry, 23*, 2710–2721. https://doi.org/10.1039/D1GC00146A

Svanberg, L., Ahrné, L., Lorén, N., & Windhab, E. (2011). Effect of sugar, cocoa particles and lecithin on cocoa butter crystallisation in seeded and non-seeded chocolate model systems. *Journal of Food Engineering, 104*, 70–80. https://doi.org/10.1016/j.jfoodeng.2010.09.023

Thakur, A., Thipparaboina, R., Kumar, D., Gouthami, K. S., & Shastri, N. R. (2016). Crystal engineered albendazole with improved dissolution and material attributes. *CrystEngComm, 18*, 1489–1494. https://doi.org/10.1039/C5CE02306H

Wang, J. P., Gallo, E., François, B., Gabrieli, F., & Lambert, P. (2017). Capillary force and rupture of funicular liquid bridges between three spherical bodies. *Powder Technology, 305*, 89–98. https://doi.org/10.1016/j.powtec.2016.09.060

Wang, K., Li, M., Wen, X., Chen, X., He, Z., & Ni, Y. (2018). Optimization of ultrasound-assisted extraction of okra (Abelmoschus esculentus (L.) moench) polysaccharides based on response surface methodology and antioxidant activity. *International Journal of Biological Macromolecules, 114*, 1056–1063. https://doi.org/10.1016/j.ijbiomac.2018.03.145

Yang, J., Wang, Y., Hao, H., Xie, C., Bao, Y., Yin, Q., Gong, J., Jiang, C., Hou, B., & Wang, Z. (2015). Spherulitic crystallization of L-Tryptophan: Characterization, growth kinetics, and mechanism. *Crystal Growth & Design, 15*(10), 5124–5132. https://doi.org/10.1021/acs.cgd.5b01089.

Yang, A., Han, Y., Pan, Y., Xing, H., & Li, J. (2017). Optimum surface roughness prediction for titanium alloy by adopting response surface methodology. *Results in Physics, 7*, 1046–1050. https://doi.org/10.1016/j.rinp.2017.02.027

Yoshiaki, K., Motonari, O., & Hideo, T. (1982). Spherical crystallization: Direct spherical agglomeration of salicylic acid crystals during crystallization. *Science, 216*, 1127–1128. https://doi.org/10.1126/science.216.4550.1127

Yu, C., Yao, M., Ma, Y., Liu, Y., Guo, S., Xu, S., Rohani, S., Chen, M., & Gong, J. (2021). Design of the spherical agglomerate size in crystallization by developing a two-step bridging mechanism and the model. *AIChE Journal, 68*, Article e17526. https://doi.org/10.1002/aic.17526

Zhao, C., Liu, Y., Ma, Y., Wu, S., & Gong, J. (2024). Optimization of green spherical agglomeration process based on response surface methodology for preparation of high-performance spherical particles. *International Journal of Pharmaceutics, 662*, Article 124515. https://doi.org/10.1016/j.ijpharm.2024.124515

Zi, G., Huang, B., Dai, M., Shi, Z., Wen, Z., Li, W., Luo, L., & Yang, L. (2022). Optimization of ammonium sulfate crystallization under ammonium nitrate based on response surface method. *Crystal Research and Technology, 58*, Article 2200246. https://doi.org/10.1002/crat.202200246